

Agglomeration and filtration of colloidal suspensions with DVLO interactions in simulation and experiment

Bastian Schäfer^a, bastian.schaefer@mvm.uka.de, ++49/1637968110

Martin Hecht^b, martin.hecht@icp.uni-stuttgart.de, ++49/71168563607

Jens Harting^{c,b}, j.harting@tue.nl, ++31/402473766

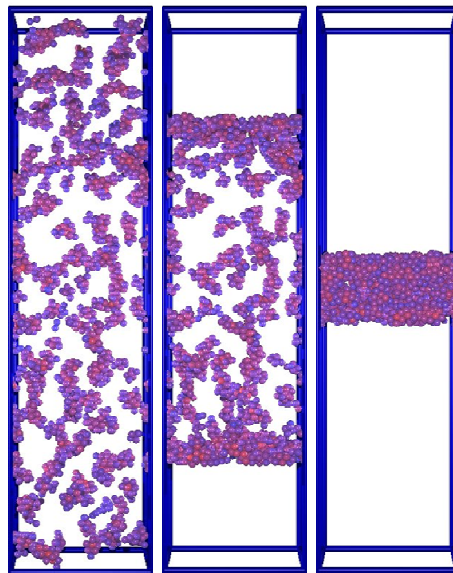
Hermann Nirschl^a, hermann.nirschl@mvm.uka.de, ++49/7216082400

^a Institut für Mechanische Verfahrenstechnik, Strasse am Forum 8, D-76128 Karlsruhe, Germany

^b Institut für Computerphysik, Pfaffenwaldring 27, D-70569 Stuttgart, Germany

^c Technische Natuurkunde, TU Eindhoven, Den Dolech 2, NL 5600 MB Eindhoven, The Netherlands

Graphical abstract



The combination of molecular dynamics (MD), stochastic rotation dynamics (SRD) and lattice Boltzmann (LB) simulations permits to study the agglomeration of colloidal particles (left), the filtration (middle) and the permeation of the compressed filter cakes (right).

1. Abstract

Cake filtration is a widely used solid-liquid separation process. However, the high flow resistance of the nanoporous filter cake lowers the efficiency of the process significantly. The structure and thus the permeability of the filter cakes depend on the compressive load acting on the particles, the particles size, and the agglomeration of the particles. The latter is determined by the particle charge and the ionic strength of the suspension, as described by the Derjaguin-Landau-Verwey-Overbeek (DLVO) theory. In this paper, we propose a combined stochastic rotation dynamics (SRD) and molecular dynamics (MD) methodology to simulate cake formation. Our method does not only allow studying the influence of the material parameters, but also accounts for long-range hydrodynamic interactions between particles. A stepwise reduction of the simulation volume leads to the formation and homogenous compression of the filter. Its permeability, as investigated with lattice Boltzmann (LB) simulations of flow through the discretized cake, depends on the particle size and porosity. Our results agree qualitatively with experimental data obtained from colloidal boehmite suspensions.

Keywords: Colloids, Agglomeration, Filtration, Molecular dynamics, Stochastic rotation dynamics, Lattice Boltzmann

2. Introduction

Cake filtration is an energy efficient and widely used solid-liquid separation process, where solid particles are retained at a filter medium or membrane and build up a filter cake with increasing thickness. The high flow resistance of nanoporous filter cakes and the growing market for fine particles demand for methods to enhance the filtration, for example by flocculating the suspensions prior to filtration. For improving the filtration processes and apparatuses, a simulation tool is required that comprehends the agglomeration of the suspension, the filtration process, and the pressure-driven permeation of the filter cakes.

Various simulation tools have been applied to different aspects of the filtration process. Some simulations are based on Darcy's law and phenomenological equations for the local porosity and local permeability of the filter cake¹⁻⁴. Kim et al. consider the aggregates as solid cores with porous shells and determine the filter cake's permeability with Stokes' equation and Brinkman's extension of Darcy's law^{5,6}. Lao et al. replace the pore system with a network of pipes and junctions and then calculate the flow in the tubes with the Poiseuille equation⁷. Eisfeld et al. propose a pseudo-continuous model for statistically described domain

geometries, where the solid/liquid interaction is represented by a coupling term in the Navier-Stokes equation⁸. Solving the Navier-Stokes equation for the complicated geometries of porous filter cakes is very time-consuming for large numbers of particles⁹. The complexity increases further if the particles are mobile¹⁰.

Molecular dynamics (MD) is the standard method for simulating the motion of discrete particles, but the simulation of suspensions is computationally far too demanding if the water molecules and ions are resolved. Even if the water is replaced by a background friction and stochastic fluctuations and only the ions are simulated explicitly, the power of today's computers would limit the simulation to only a few colloidal particles. Omitting the water molecules and ions and assuming that every particle collision leads to agglomeration reduces the computational effort significantly, but this approach does not include electrostatic interactions¹¹. Their influence is considered in Monte Carlo studies on the porosity and cake structure of filter cakes¹². Barcenas et al. present a simple way to control the particle agglomeration in Monte Carlo simulations: the suspension is represented by a two-component mixture of colloidal particles and inhibitor particles¹³. Yu et al. perform Monte Carlo simulations based on the fractal nature of the pore size distribution in porous media¹⁴.

Alternative methods to simulate mobile particles in suspensions became popular in recent years: Brownian dynamics simulations include Brownian motion, but the hydrodynamics is reduced to a simple Stokes force¹⁵⁻¹⁸. Stokesian dynamics include multiparticle hydrodynamic interactions, but the numerical effort increases with the third power of the particle number¹⁹. This problem can be reduced by using accelerated Stokesian dynamics²⁰.

Another popular approach is to combine MD simulations of the solid particles with a simulation of the liquid, for example based on the Navier-Stokes equations, dissipative particle dynamics, the lattice Boltzmann (LB) method or stochastic rotation dynamics (SRD). In these methods, the numerical effort for calculating the hydrodynamic interactions grows linear with the particle number²¹.

Dissipative particle dynamics comprise the hydrodynamics and Brownian motion²². The lattice Boltzmann method is a powerful tool for modelling single and multiphase flow, which was extended to simulate particle agglomeration including Brownian motion^{23, 24}. SRD is an efficient simulation method based on a simple algorithm that includes thermal noise and hydrodynamic interactions of a real fluid²⁵⁻²⁸. The method is also known as multi particle collision dynamics. It has been successfully applied to colloidal suspensions²⁹⁻³¹ and flow in confined geometries^{30, 32, 33}.

We approach the agglomeration and filtration of colloidal suspensions with a combination of SRD for the electrolyte solution and MD for the colloidal particles. The MD simulation includes the particle-particle interactions as described by the DLVO theory^{34, 35}. The permeability of the fixed structure of the filter cake is investigated with the LB method. The methods are explained in detail in chapter 4, including the boundary conditions which represent the filter cell. The article also presents the theoretical background of filter cake formation and permeation in chapter 3. The numerical data are compared to experimental results in chapter 5.

3. Theoretical background

Filtration processes are commonly described by Darcy's equation for the flow rate of the filtrate^{1, 36, 37}

$$\dot{V}_L = \frac{A_c}{\eta} \frac{\Delta p}{R_F}, \quad (1)$$

with the cross-section area of the filter cake A_c , the dynamic viscosity of the permeate η , and the driving pressure difference Δp . Neglecting the membrane resistance, the flow resistance:

$$R_F = \frac{h_c}{K} \quad (2)$$

is the ratio of the thickness of the filter cake h_c to its permeability K . The permeability mainly depends on the particle size and the porosity of the filter cake Φ , that is the ratio of the liquid volume V_L to the total volume of the filter cake $A_c h_c$. The porosity depends on the particle size, the filtration pressure, and the agglomeration of the particles^{38, 39}. The agglomeration is determined by the DLVO interactions between the particles, as described below.

Particles in most aqueous suspensions carry a surface charge, but the effects of the surface charge are only significant for small particles with a large specific surface area. The charge results from a dissociation of ions on the particles' surface. The equilibrium of the dissociation depends on the concentration of hydroxide and oxonium ions if no specifically adsorbing ions are present. The particle charge is positive at low pH values and negative at high pH values. The material specific pH value where the surface charge equals zero is called isoelectric point (IEP)^{40, 41}. The charged particle is surrounded by an electrochemical double layer (EDL), a diffuse cloud of oppositely charged ions attracted from the surrounding liquid by the Coulomb force. The EDL can be partly sheared off by a relative motion between the particle and the liquid. The electric potential difference between the shear plane and the

surrounding liquid, the so-called zeta potential ζ , is the most common measure for the surface charge, since the surface charge density itself can only be determined by laborious titrations⁴².

According to the well-established DLVO theory, a suspension's stability against agglomeration is determined by the sum of the potentials of the London-van-der-Waals attraction, the Born repulsion, and the screened electrostatic Coulomb repulsion, which depends on the zeta potential and the ionic strength of the suspension. For a pair of round particles, the van-der-Waals potential can be written as^{43,44}

$$\Psi_{vdW}(d) = -\frac{A_H}{12} \left[\frac{d_p^2}{d^2 - d_p^2} + \frac{d_p^2}{d^2} + 2 \ln \left(\frac{d^2 - d_p^2}{d^2} \right) \right], \quad (3)$$

with the Hamaker constant A_H , the particle diameter d_p and the center-to-center distance $d = x_m - x_n$ between particles with positions x_m and x_n . The Coulomb potential Ψ_{Coul} for a pair of identically charged spheres is^{41,44}

$$\Psi_{Coul} = \pi \epsilon_{rel} \epsilon_0 \left[\frac{2 + d_p}{1 + d_p \kappa} \cdot \frac{4k_B T}{ze} \tanh \left(\frac{ze\zeta}{4k_B T} \right) \right]^2 \frac{(d_p)^2}{d} \exp(-\kappa[d - d_p]), \quad (4)$$

with the vacuum permittivity ϵ_0 , the relative permittivity ϵ_{rel} , the Boltzmann constant k_B , the temperature T , the elementary charge e and the valency of the ions z . The reciprocal Debye length^{41,44}

$$\kappa = \left(\frac{2F^2 I}{\epsilon_{rel} \epsilon_0 N_A k_B T} \right)^{\frac{1}{2}} \quad (5)$$

is a function of the ionic strength I , with the Faraday constant F and the Avogadro constant N_A . The short-ranging Born repulsion reflects Pauli's principle which states that the electron orbitals of adjacent molecules cannot occupy the same state and thus keeps the particles from penetrating each other. In this study, the short-ranging Born repulsion is replaced by a less steep Hertz force, which is discussed below.

The DLVO theory explains the stability of colloidal particles almost quantitatively^{41,44}. The superposition of the attractive and repulsive potentials results in the DLVO potential with material specific minima and maxima. Figure 1 shows plots of the DLVO potential for illustrative combinations of surface charge and ionic strength.

- For a low zeta potential or a high ionic strength, the van-der-Waals attraction is stronger than the Coulomb repulsion at every inter-particle distance, leading to a monotonic decrease of the potential energy upon the approach of two particles.

Consequently, the system is unstable and the particles will agglomerate. The Born repulsion keeps the particles apart at very short distances.

- If the ionic strength is low and the zeta potential is high or intermediate, the Coulomb repulsion is stronger than the van-der-Waals attraction for a region of the inter-particle distance. This forms an energy barrier against a further approach of the particles. According to equipartition principle of statistical physics, the particles' kinetic energy is Boltzmann distributed and the average energy of the particles amounts to $1.5 k_B T$ ⁴⁵. Consequently, a range from rapid to slow agglomeration is found for increasing energy barriers. The small secondary energy minimum outside of the energy maximum is too shallow to hold back particles against mechanical load^{41, 44}.
- For an intermediate ionic strength and a high or intermediate zeta potential, the secondary minimum is deeper than $2 k_B T$. The particles can be captured in the minimum and thus form secondary agglomerates. These are less stable than primary agglomerates because of the significantly smaller energy minimum.

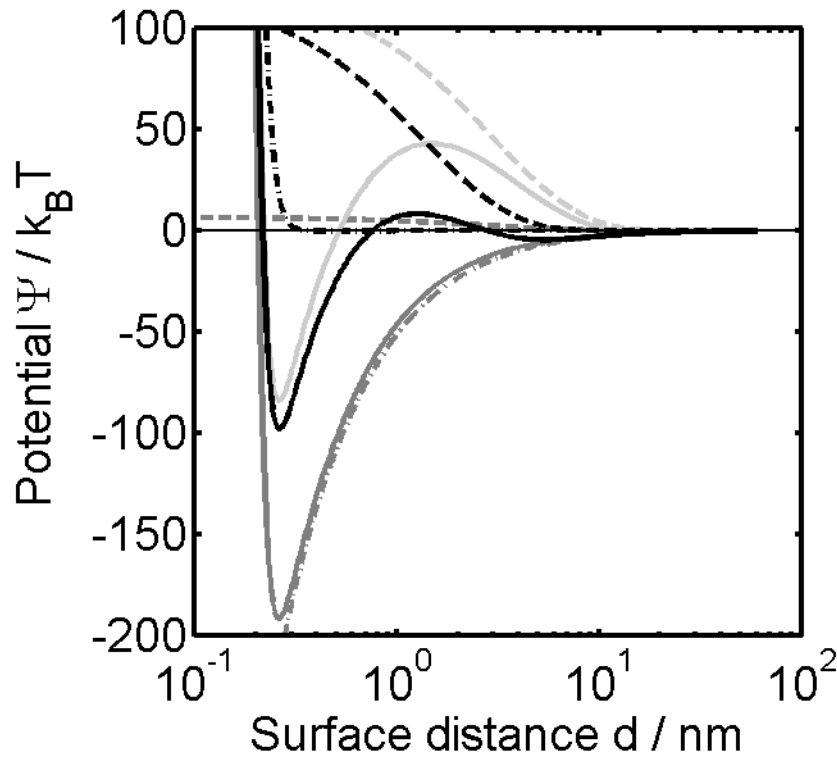


Figure 1: Interaction potentials for particles with a diameter of 120 nm: van-der-Waals potential (dark-grey, dashed-dotted line), Born potential (black dashed-dotted line), Coulomb potentials (dashed lines,

dark grey: $\zeta = 10$ mV, $I = 0.01$ mol/L, light grey: $\zeta = 45$ mV, $I = 0.01$ mol/L, black: $\zeta = 45$ mV, $I = 0.05$ mol/L), and DLVO potentials (solid lines, dark grey: $\zeta = 10$ mV, $I = 0.01$ mol/L, light grey: $\zeta = 45$ mV, $I = 0.01$ mol/L, black: $\zeta = 45$ mV, $I = 0.05$ mol/L).

The filtration behavior, pore structure, and permeability of a filter cake depend significantly on the presence and size of agglomerates in the suspension. Agglomerated suspensions lead to loosely textured packed beds with large pores between the agglomerates. The agglomerates can be considered as large particles with an internal porosity and so-called macro-pores between the agglomerates which are accountable for the high permeability³⁷. In contrast, packed beds formed from stable suspensions with high surface charge have a dense structure with a homogeneous pore size distribution, a low porosity, and a low permeability⁴. The filterability can thus be increased by changing the pH value in the direction towards the IEP or by increasing the ionic strength of the suspension.

Porosity and permeability of nanoporous filter cakes further depend on the filtration pressure⁴⁶. Filter cakes from agglomerated suspensions are highly compressible because the agglomerates can be easily deformed. The rearranging of the particles mainly reduces the size of the large pores between the agglomerates^{4, 47, 48}, which are accountable for the major part of the fluid transport. Consequently, the compression of the macropores between the agglomerates has a large effect on the permeability, even if a large porosity remains inside the agglomerates⁴. Filter cakes formed from stable suspensions are less compressible because of the lack of interagglomerate pores. As shown by Singh et al., the compressibility of filter cakes from colloidal silica spheres slightly decreases with increasing ionic strength as long as it stays below the critical coagulation concentration⁴⁹.

The agglomerate structure can be described with the pair correlation function

$$G(d) = \frac{V}{N^2} \left\langle \sum_n \sum_{n \neq m} \delta(d - |\mathbf{x}_m - \mathbf{x}_n|) \right\rangle, \quad (6)$$

with the examination volume V and the number of particles in that volume N . It gives the probability for the particles to find another particle at a certain center-to-center distance d . The peaks of G indicate regular structures, for example a peak at two particle radii originates from particles in direct contact and peaks at larger distances show more complex structures⁵⁰.

4. Simulation methods

For simulating the agglomeration and filtration, the motion of the spherical particles is calculated with a molecular dynamics (MD) simulation, whereas the fluid is simulated with stochastic rotation dynamics (SRD), which is described below. Newton's equation of motion

is solved for each MD particle by a velocity Verlet algorithm⁵⁰. The thermal contribution to the kinetic energy of the MD and SRD particles is controlled with a Monte Carlo thermostat described in²⁷ to ensure a simulation at constant temperature.

The simulation starts with 2000 MD-particles that are stochastically distributed in the simulation space. To obtain a volume concentration of 3.7%, which is consistent with the experiments, the system dimensions are set to 76.8 particle diameters in the vertical direction of compression and 19.2 particle diameters in the horizontal directions. The boundaries in the horizontal directions are periodic, while the closed boundaries in the vertical direction exert a Hooke force on overlapping particles. Simulations with 4000 particles yield comparable porosities of the packed beds, so that finite-size effects are excluded.

The particles agglomerate until an equilibrium structure is reached (see figure 2, left), as controlled by analyzing the temporal development of the pair correlation function G . Subsequently, the filtration takes place by incrementally approaching the z-boundaries of the MD-space towards each other. Consequently, the MD particles build up filter cakes on the top and bottom boundary conditions, like on the membranes in a two-sided filtration apparatus (see figure 2, center). After both filter cakes merge, they are compressed between the membranes (see figure 2, right) until the Hooke force between the z-boundaries and the MD particles reaches the desired compressive load. Like in reality the compression is carried by the particle network. The fixed positions of the particles define the geometry of the porous structures, which are further examined using the lattice Boltzmann (LB) method.

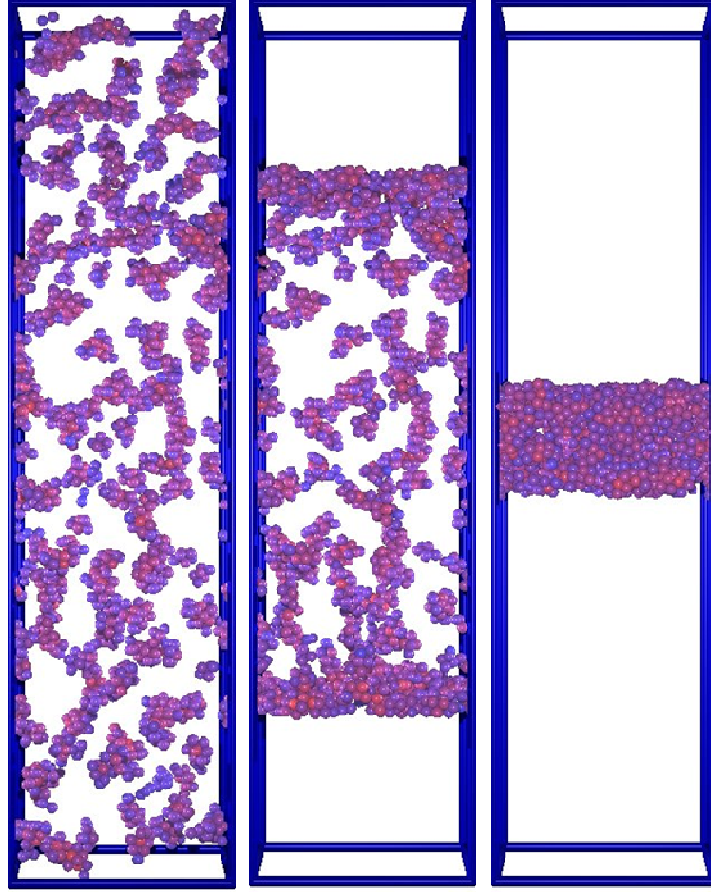


Figure 2: MD particles in the simulation space at different stages of the simulation (left: agglomeration, center: filtration, right: compression). The SRD particles and the MD boundaries are not visible.

4.1. MD simulation of the particles

The motion of the particles is calculated with a velocity Verlet algorithm, using Newton's equation of motion

$$\mathbf{F}_m = m_m \ddot{\mathbf{x}}_m, \quad (7)$$

with the force \mathbf{F}_m , the mass m_m , and the acceleration $\ddot{\mathbf{x}}_m$ for each particle m . To reduce the computational effort, the MD simulation space is mapped with a cubic grid that has a grid constant of 4 particle radii and the particle interactions are restricted to MD particles in the same and adjacent cells. The interaction force is the derivative of the interaction potentials introduced above, including the van-der-Waals attraction and the Coulomb repulsion. In order to reduce the potential gradients and thus expand the simulation time step, the Born potential, which keeps the particles from overlapping, is replaced by the less steep Hertz potential

$$\Psi_{\text{Hertz}} = K_{\text{Hertz}} \cdot (d_p - d)^{2.5}, \quad (8)$$

for $d < d_p$ with the Hertz constant $K_{\text{Hertz}} = 0.1$. The particles can consequently overlap to a small extend, but since the overlap is relatively small, its influence on the structure of the

filter cake can be neglected. The van-der-Waals potential is cut-off for inter-particle distances below 0.005 radii to circumvent its singularity at direct contact. The gap between the cut-off radius and the particle surface is modeled by a Hooke law with a coefficient D_H of $7.7 \cdot 10^6$ N/m. The coefficient is chosen such that the potential is steadily differentiable at the transition point between the Hooke law and the DLVO potential. The resulting potential in the simulations agrees very well with the real potential in the range of inter-particle distance that determines the agglomeration.

The resistance of the viscous fluid against the relative motion between two particles is not properly reproduced by the SRD simulation at small particle distances. This shortcoming is corrected by the dissipative lubrication force²⁹

$$F_{Lub} = -(\dot{\mathbf{x}}_m - \dot{\mathbf{x}}_n) \frac{6\pi c_{Lub} \eta}{d + r_{CO,i} - d_p} \left(\frac{d_p}{4} \right)^2, \quad (9)$$

with the particle velocities $\dot{\mathbf{x}}_m$ and $\dot{\mathbf{x}}_n$, the lubrication constant c_{Lub} and inner cut-off radius $r_{CO,i}$ to exclude the singularity for touching particles. The lubrication constant of $c_{Lub} = 0.2$ is adjusted to reproduce the stability diagram presented in figure 7.

4.2. SRD simulation of the liquid

The SRD method introduced by Malevanets and Kapral²⁵ is used for simulating the fluid because it intrinsically contains fluctuations, has low demands for computational time and is applicable to colloidal suspensions^{22, 28, 29, 31, 51}. SRD is based on calculating the continuous positions of virtual fluid particles at the time $t + \Delta t_{SRD}$ from the previous positions $\mathbf{x}_m(t)$ and velocities $\dot{\mathbf{x}}_m(t)$:

$$\mathbf{x}_m(t + \Delta t_{SRD}) = \mathbf{x}_m(t) + \Delta t_{SRD} \cdot \dot{\mathbf{x}}_m(t). \quad (10)$$

Since the particles are pointlike, they cannot collide. Instead, momentum is exchanged between the SRD particles in a collective interaction step: the SRD particles are sorted into cubic cells with the length L_{Cell} . Within each cell k , the relative velocities of the particles $\dot{\mathbf{x}}_m(t) - \dot{\bar{\mathbf{x}}}_k(t)$ with respect to their average velocity $\dot{\bar{\mathbf{x}}}_k$ are rotated according to⁵²

$$\dot{\mathbf{x}}_m(t) = \dot{\bar{\mathbf{x}}}_k(t) + \Omega_{SRD,k}(t) \cdot [\dot{\mathbf{x}}_m(t) - \dot{\bar{\mathbf{x}}}_k(t)]. \quad (11)$$

The rotation matrix $\Omega_{SRD,k}$ is stochastically chosen for each cell and time step from a set of six possible rotations by $+90^\circ$ or -90° around the three coordinate axes. This is a mathematically simple means to exchange momentum between the fluid particles while

conserving the total mass, energy, and momentum within each cell. If the mean velocity is interpreted as the streaming velocity of the fluid in each cell, the relative velocities represent the thermal fluctuations. Since the rotation does not affect the mean velocity of the fluid particles, the total momentum and the kinetic energy of the streaming velocity do not change. Also the kinetic energy associated to thermal fluctuations remains constant, because the rotation of the thermal fluctuations does not influence their magnitude. The solid particles from the MD simulation are coupled to the SRD simulation by including them in the rotation step. The different masses m_m of the MD and SRD particles have to be considered as weighting factor when calculating the mean velocities in the cells

$$\dot{\bar{\mathbf{x}}}_k(t) = \sum_{m=1}^{N_k(t)} \dot{\mathbf{x}}_m(t) m_m / \sum_{m=1}^{N_k(t)} m_m, \quad (12)$$

with the number of particles $N_k(t)$ in the cell k ²⁷.

If the particle velocities are small, so that most particles remain in their cell, neighboring particles are correlated over several time steps. This correlation is broken if the particles are observed from a moving inertial system with a moving grid. The simulation is thus not Galilean-invariant, which would require that an experiment is independent of the inertial frame from which it is observed. However, in SRD simulations these correlations are minimized if the mean free path of the SRD particles

$$\lambda = \Delta t_{SRD} \sqrt{k_B T / m_{SRD}} \quad (13)$$

is chosen to be at least half the length of the SRD cells, where the mass of one SRD particle is given by

$$m_{SRD} = \frac{L_{Cell}^3 \rho_L}{\langle N_k \rangle}, \quad (14)$$

and ρ_L denotes the liquid density ⁵². Therefore, under this condition, Galilean invariance is restored. In this study, the average number of SRD particles per cell is chosen as $\langle N_k \rangle = 60$, the length of the SRD cells is given in table 1.

4.3. *Scaling of the simulation parameters*

To translate an MD particle by a distance of one diameter, each force or process in the system takes a different characteristic time that depends on the particle diameter d_p (see the solid lines in figure 3). The time τ_{Sed} it takes for an MD particle to sediment a distance of one particle diameter is reciprocal to the Stokes velocity v_{Sed}

$$\tau_{Sed} = \frac{d_p}{v_{Sed}} = \frac{18\eta}{d_p g (\rho_s - \rho_L)}, \quad (15)$$

with the gravitational constant g , the liquid density ρ_L , and the particle density ρ_s . It is thus inversely proportional to the particle diameter d_p . The time τ_{Diff} it takes a particle to diffuse a distance of one particle diameter depends on the diffusion constant D and is proportional to the third power of the diameter⁵³:

$$\tau_{Diff} = \frac{d_p^2}{2D} = \frac{3\pi\eta d_p^3}{2k_B T}. \quad (16)$$

The average velocity of the particles' thermal fluctuations τ_{TF} refers to a kinetic energy of $1.5 k_B T$ ⁵⁴, leading to a characteristic time of

$$\tau_{TF} = \sqrt{\frac{d_p^5 \pi \rho_s}{18 k_B T}}. \quad (17)$$

The particle relaxation time

$$\tau_p = \frac{1}{18} \frac{d_p^2 \rho_s}{\eta} \quad (18)$$

is the time for a particle to adapt to the flow field of the surrounding fluid. The distortions of the liquid flow field relax with a characteristic time

$$\tau_L = \frac{d_p^2 \rho_L}{2\eta}. \quad (19)$$

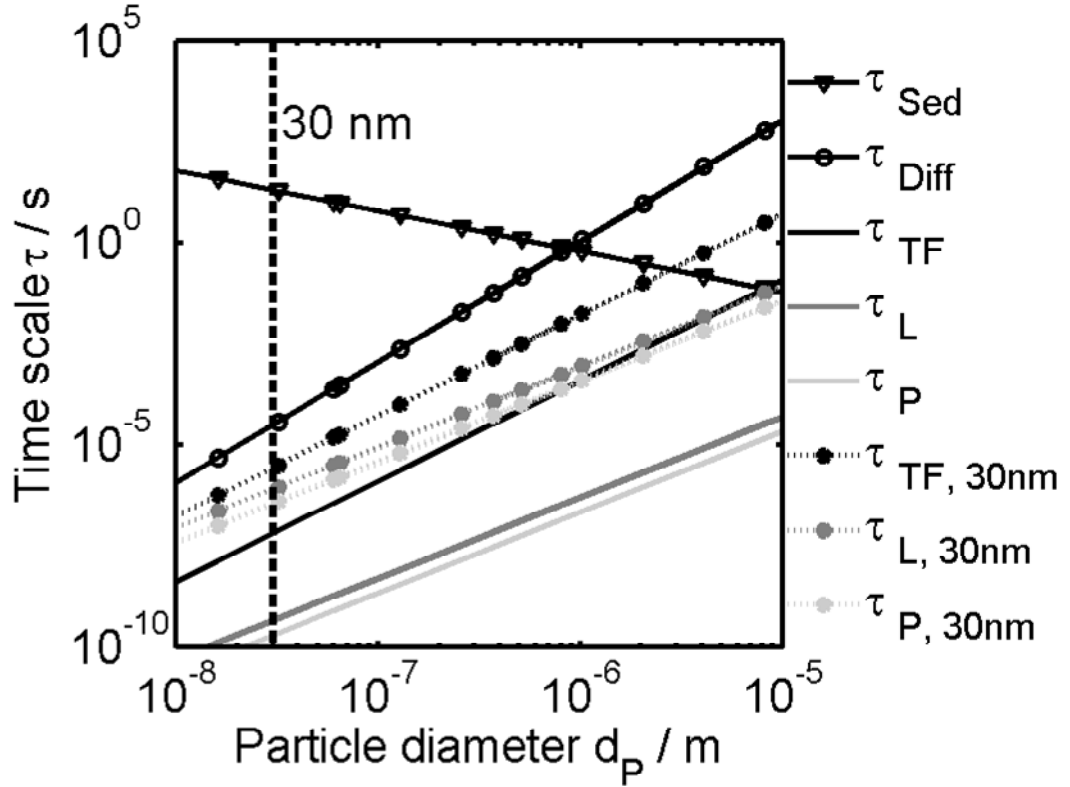


Figure 3: Characteristic times for different forces in the simulation before scaling (solid lines) and after scaling for a particle diameter of 30 nm (dotted lines). The symbols are explained in the text.

Since the smallest characteristic time determines the maximum simulation time step needed to maintain numerical stability, the numerical effort increases for a decreasing particle size. The simulation of colloidal suspensions is thus limited by the power of today's computers. However, the characteristic times can be modified while maintaining the physical behavior of the suspension if the physical properties of the system are carefully scaled. This scaling must not change the sequence of the characteristic times or bring them close together. Each time scale ratio represents a characteristic number of the system. Examples are the Reynolds number $Re = \tau_L / \tau_{Sed}$, the Archimedes number $Ar = (9\tau_L) / (2\tau_{Sed})$, the Schmidt number $Sc = \tau_{Diff} / \tau_L$, the Péclet number $Pe = \tau_{Sed} / \tau_{Diff}$. The major physical behavior of the system is not influenced by an alteration of these numbers as long as they remain much smaller or much larger than one, which means that the two corresponding forces do not compete. The scaling must be done carefully for each particle diameter since the latter influences the characteristic time scales. In the example shown in figure 3, the ratio between τ_L and τ_P is identical for the original system (solid lines) and the system scaled for particles of 30 nm (dotted lines). τ_{Sed} and τ_{Diff} are not affected by the scaling.

The SRD simulation used in this study involves a coarse-graining which is accompanied by a scaling of the fluid viscosity. For the rotation angles of $\pm 90^\circ$, the viscosity of the SRD fluid is

$$\eta_{SRD} = \rho_L \left(\frac{L_{Cell}^2}{18\Delta t_{SRD}} \left(1 - \frac{1 - e^{-\langle N_k \rangle}}{\langle N_k \rangle} \right) + \frac{k_B T_{SRD} \Delta t_{SRD}}{4m_{SRD}} \frac{\langle N_k \rangle + 2}{\langle N_k \rangle - 1} \right), \quad (20)$$

with the temperature of the SRD fluid T_{SRD} . To reproduce the realistic diffusion of the solid particles, the diffusion constant in the simulation

$$D = \frac{k_B T_{SRD}}{3\pi\eta_{SRD}d_p}, \quad (21)$$

including the viscosity of the SRD fluid η_{SRD} , is identified with the real diffusion constant given in table 1. With $\lambda = L_{Cell}/2$ to guarantee Galilean invariance⁵², equations (13), (14), (20), and (21) lead to the time steps and scaling factors given in table 1. To preserve the sedimentation velocity and diffusion constant, the gravitational constant and the temperature are scaled by the same factor as the viscosity. Also, the inter-particle forces are scaled to maintain their ratio to the energy associated to the thermal fluctuations of particles. The resulting SRD time steps are too large to resolve the motion of the colloidal particles, so that a smaller time step is chosen for the MD simulations. The SRD-calculation is applied less often than the MD calculation, which reduces the computational time substantially.

Table 1: Simulation parameters for different particle diameters

Particle diameter / nm	30	70	120
Length of the SRD cells / nm	25	50	100
Diffusion constant / m ² /s	$1.44 \cdot 10^{-11}$	$6.17 \cdot 10^{-12}$	$3.60 \cdot 10^{-12}$
Scaled temperature / K	$1.67 \cdot 10^{-1}$	$8.34 \cdot 10^{-2}$	$4.17 \cdot 10^{-2}$
SRD time step / s	$1.25 \cdot 10^{-7}$	$1.10 \cdot 10^{-6}$	$8.50 \cdot 10^{-6}$
Scaling factor	$5.66 \cdot 10^{-4}$	$2.828 \cdot 10^{-4}$	$1.414 \cdot 10^{-4}$
MD time step / s	$1 \cdot 10^{-10}$	$1 \cdot 10^{-9}$	$1 \cdot 10^{-9}$

4.4. Determination of the permeability by lattice Boltzmann simulations

The lattice Boltzmann (LB) method is a mesoscopic approach to simulate the motion of viscous fluids. The fluid is represented by particle populations located on the nodes of a lattice and the velocity space is discretized to only a few basic lattice vectors \mathbf{e}_j . These are the main lattice directions \mathbf{e}_1 to \mathbf{e}_6 , the diagonals \mathbf{e}_7 to \mathbf{e}_{18} , and the rest vector \mathbf{e}_{19} (see figure 4). Fluid motion is described by the single-particle distribution functions $f_j(\mathbf{x}, t)$, which give the expected number densities of particles moving along the lattice vectors \mathbf{e}_j for each lattice site \mathbf{x} and time t and which is depicted by the grey polyhedron in figure 4.

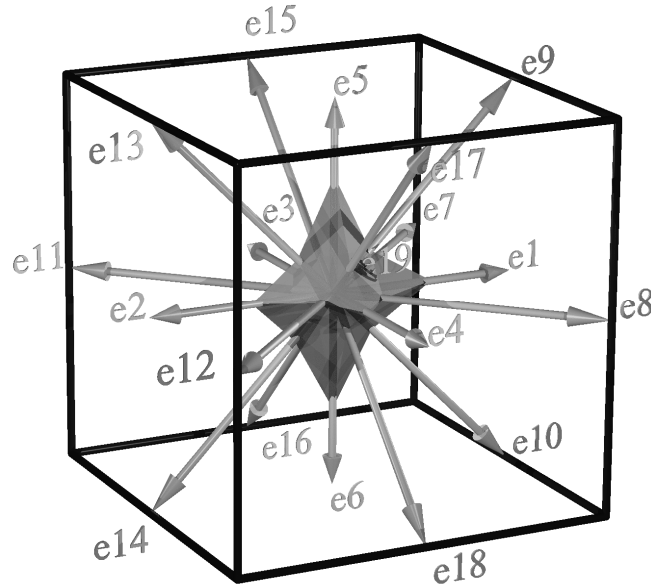


Figure 4: Computational lattice of a three-dimensional lattice Boltzmann simulation with the lattice vectors \mathbf{e}_j and the distribution functions f_j for each lattice vector depicted by the grey polyhedron.

During each time step Δt_{LB} , the particle distributions are propagated to the next lattice site $\mathbf{x} + \mathbf{e}_i$, as described by the discretized Boltzmann equation^{55, 56}

$$f_j(\mathbf{x} + \mathbf{e}_j, t + \Delta t_{LB}) = f_j(\mathbf{x}, t) + \Delta t_{LB} \Omega_{LB,j}(f(\mathbf{x}, t)). \quad (22)$$

In this study, the time step Δt_{LB} and the lattice constant Δx are set to 1 for the sake of simplicity. The collision operator $\Omega_{LB,j}$ mimics the viscous behavior of the fluid by relaxing it towards equilibrium. It exchanges momentum between the fluid particles while conserving mass, momentum, and energy. In the Bhatnagar-Gross-Krook algorithm⁵⁷, which is used in this study, the collision operator is given by

$$\Omega_{KB,j}(\mathbf{x},t) = -\frac{1}{\tau_{LB}}(f_j(\mathbf{x},t) - f_j^{eq}(\mathbf{x},t)), \quad (23)$$

with the relaxation time $\tau_{LB} \approx 1$. The equilibrium distribution function f_j^{eq} is the second order Taylor expansion around a local equilibrium of the Boltzmann equation⁵⁸

$$f_j^{eq}(\mathbf{x},t) = w_j \frac{\rho_{LB}}{\rho^\circ} \left(1 + \frac{\mathbf{v}_{LB} \cdot \mathbf{e}_j}{c_s^2} + \frac{(\mathbf{v}_{LB} \cdot \mathbf{e}_j)^2}{2c_s^4} - \frac{\mathbf{v}_{LB} \cdot \mathbf{v}_{LB}}{2c_s^2} \right), \quad (24)$$

with the lattice weights w_j to correct for the discrepancy between the length of the lattice vectors, the reference density ρ° , the local density

$$\rho_{LB}(\mathbf{x},t) = \rho^\circ \sum_{j=1}^{19} f_j(\mathbf{x},t), \quad (25)$$

the local macroscopic velocity

$$\mathbf{v}_{LB}(\mathbf{x},t) = \frac{\sum_{j=1}^{19} f_j(\mathbf{x},t) \mathbf{e}_j}{\sum_{j=1}^{19} f_j(\mathbf{x},t)}, \quad (26)$$

and the speed of sound

$$c_s = \frac{1}{\sqrt{3}}. \quad (27)$$

In the context of this study, the LB simulation can be seen as a Navier-Stokes solver based on a very simple algorithm that is capable to cope with complex flow domains⁵⁸⁻⁶⁰. LB simulations are applicable to liquid flow in nanoporous filter cakes since the relevant characteristic numbers, i.e. the Reynolds number Re , the Mach number Ma and the Knudsen number Kn , are well below one for both the experiment and the simulation. The LB method is ideally suited for simulating fluid flow in porous media since it provides a simple method to represent the complicated pore geometry: the so-called mid-grid bounce back condition is a common way to implement no-slip boundary conditions on the surface of the porous sample⁶¹⁻⁶³. Since the boundary conditions are imposed locally, even complex boundaries do not significantly increase the computational time⁶⁴. Furthermore, LB simulations are easy to parallelize because locally only information of the nearest neighbor nodes is required⁶².

The fixed geometries of the filter cakes, as obtained from the MD- and SRD-simulation, are mapped on a cubic lattice with 128 nodes in each direction. The number of nodes in the direction of permeation follows from the thickness of the filter cake. The compressed filter cake is centered in the computational domain, so that above and below a fluid reservoir is

present to ensure that a homogeneous in- an out-flow pressure is applied and the flow field can adopt to the complex pore network ⁵⁵. The hydraulic force that drives the permeation is applied to a layer of nodes in the inlet reservoir by adding the additional term

$$\boldsymbol{\varphi}_j = w_j \frac{1}{\rho_{LB} c_s^2} \mathbf{b} \cdot \mathbf{e}_j, \quad (28)$$

to the right side of equation (23), with the external force density \mathbf{b} ⁶⁵. An additional force term also has to be added to equation (26)

$$\mathbf{v}_{LB}(\mathbf{x}, t) = \frac{\sum_{j=1}^{19} f_j(\mathbf{x}, t) \mathbf{e}_j}{\sum_{j=1}^{19} f_j(\mathbf{x}, t)} + \frac{\mathbf{b}}{2\rho_{LB}(\mathbf{x}, t)} \quad (29)$$

to satisfy the Navier-Stokes equation using the Chapman-Enskog expansion ⁶⁶⁻⁶⁸. The permeability of the filter cake is calculated from the difference of the pressure in the inlet and outlet reservoir, calculated as

$$p(\mathbf{x}, t) = c_s^2 \rho_{LB}(\mathbf{x}, t), \quad (30)$$

and the fluid's velocity in the direction of flow, averaged over the whole sample.

5. Experiments

The experiments are performed in an Electro-Compression-Permeability-Cell, which is described in detail in ^{69, 70}. The Electro-Compression-Permeability-Cell is designed for the filtration of colloidal suspensions between two membranes with a cross section area of 0.005 m² in a cylindrical tube. The particles in the suspensions agglomerate according to their surface charge and the ionic strength of the suspensions. In analogy to the simulation set-up, the particles are retained by the membranes and build up a filter cake, while the liquid can drain through the filter cake and the membrane. To obtain a homogenous structure, the filter cake is compressed between the membranes by the force of a plunger until the equilibrium thickness between 3 mm and 8 mm is reached. Applying a pressure of 20 kPa to a liquid reservoir on the upstream side of the filter cake drives the liquid through the filter cake onto a scale on the downstream side ⁶⁹.

For each pH value and ionic strength a new filter cake is formed. The suspensions are prepared by dispersing 25 g of boehmite particles (Disperal®, Disperal 20® or Disperal 40® from Sasol, Germany) in 225g potassium nitrate solution with the desired ionic strength and a pH value of 2.7. The pH value is subsequently adjusted by adding caustic potash. Disperal®, Disperal 20® and Disperal 40® were chosen for the experiments because they have the same

chemical composition, but different particle sizes. The number-weighted mean diameter $d_{50,0}$ of the dispersed primary particles is 24 nm for Disperal®, 73 nm for Disperal 20®, and 130 nm for Disperal 40®, as measured with a Nanotracer from Mircotrac Inc., USA. Boehmite has an isoelectric point (IEP) at a pH value of 9.5.

6. Results

The simulation methods introduced above are used to investigate the influence of the particle size, the particle charge, and the ionic strength of the suspension on the filtration of suspensions and the permeability of the resulting filter cakes. The colloidal particles in the suspensions agglomerate according to the DLVO theory. Subsequently, the filtration of the suspension is started by reducing the simulation space of the particles. After the filter cakes are compressed to their equilibrium thickness, a lattice Boltzmann simulation yields their permeabilities K .

6.1. Agglomeration of the particles

The formation of agglomerates, which dominates the filtration behavior of the suspension and the permeability of the filter cakes, depends on whether the kinetic energy of the particles is sufficient to overcome the energy maximum in the DLVO potential. The averaged energy of the thermal degrees of freedom of the simulated particles equals $1.5 k_B T$ for the three-dimensional simulations, which is consistent with the theory. Furthermore, the viscosity of the liquid, as calculated from the Stokes-Einstein relation

$$\eta = \frac{k_B T}{3\pi d_p D}, \quad (31)$$

agrees with the viscosity of water. The diffusion constant of the molecular dynamics (MD) particles is calculated as

$$D = \frac{\sum_{m=1}^{N_{MD}} (\mathbf{x}_m(t) - \mathbf{x}_m(t_0))^2}{2N_{MD}(t - t_0)}, \quad (32)$$

with the number of MD particles N_{MD} .

The agglomeration of the particles is analyzed by means of the pair correlation function $G(d)$, which is shown in figure 5 for the different particle diameters. The peaks refer to the center-to-center distance of the dark spheres in figure 5. Similar pair correlation functions are observed in Brownian Dynamics simulations¹⁶. The gap of G between 2 and 2.2 radii

indicates the low probability of finding a particle in this steep region of the DLVO potential of another particle. The extension of the first peaks to less than two radii indicates an overlapping of the particles. This results from substituting the Born repulsion by the Hertz force in the DLVO interactions in order to reduce the potential gradient and the computational time. The resulting broadening of the peaks is especially pronounced for the small particles, since the penetration depth is related to the particle radius. The broadening effect is accompanied by a smaller peak height since the integral has to be conserved.

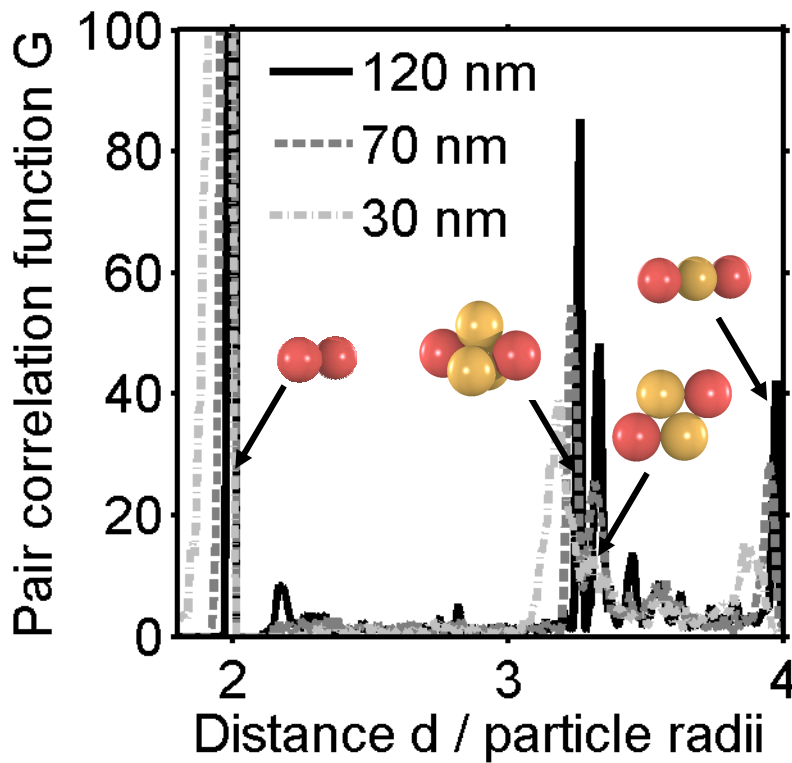


Figure 5: Pair correlation function $G(d)$ for particles of different diameters with sketches of the structures that are represented by the peaks. The peak positions refer to the distance between the dark spheres.

The position of the peaks is used to detect primary and secondary agglomeration and to distinguish between them. For secondary agglomerates, the peaks of G are at larger distances than for primary agglomerates (see figure 6) because the secondary minimum is at a larger surface distance. Furthermore, the peaks for secondary agglomerates are significantly broader due to the larger width of the secondary minimum. This indicates a higher mobility of the particles in the agglomerates. Secondary agglomerates are thus less stable against deformation. For secondary agglomerates, the higher order peaks of G are less pronounced.

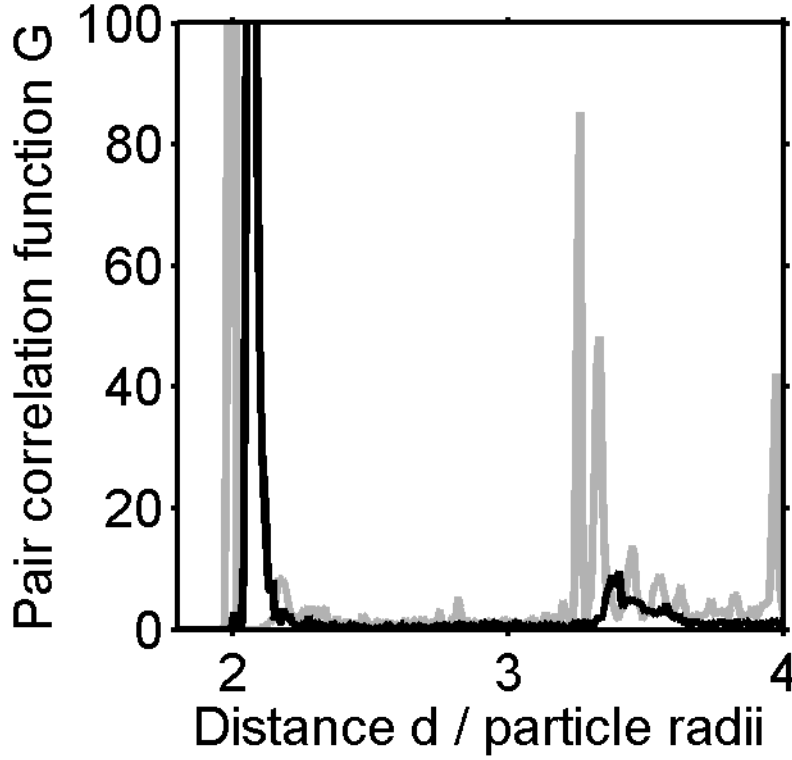


Figure 6: Pair correlation functions $G(d)$ for a particle diameter of 120 nm in the presence of primary agglomerates (grey) and secondary agglomerates (black).

The stability diagram (see Figure 7) shows the agglomeration behavior of suspensions with different particle diameters for all combinations of zeta potential ζ and ionic strength I . For combinations above and between the solid lines, the difference between the maximum and the secondary minimum of the DLVO potential is smaller than $10 k_B T$. The energy barrier should be overcome by at least some of the particles, which have a Boltzmann distributed kinetic energy⁴⁵. Between the solid lines and the dashed lines, the energy barrier is higher than $10 k_B T$ and the secondary minimum is deeper than $2 k_B T$, so that some particles get caught in the secondary minimum. The suspensions are stable below the dashed lines, where the secondary minimum is too shallow to retain the particles. The particle size has a stronger influence on secondary agglomeration than on primary agglomeration.

The symbols show the state of agglomeration observed in the simulations for particle diameters of 30 nm (black symbols), 70 nm (dark grey symbols), and 120 nm (light grey symbols). The data points for a diameter of 70 nm are shifted vertically for the sake of optical clarity, since they would normally have the same positions like the data points for 120 nm. Primary agglomerates are indicated by triangles, secondary agglomerates by circles and

unagglomerated suspensions by crosses. The agglomeration behavior observed in the simulations agrees with the stability diagram.

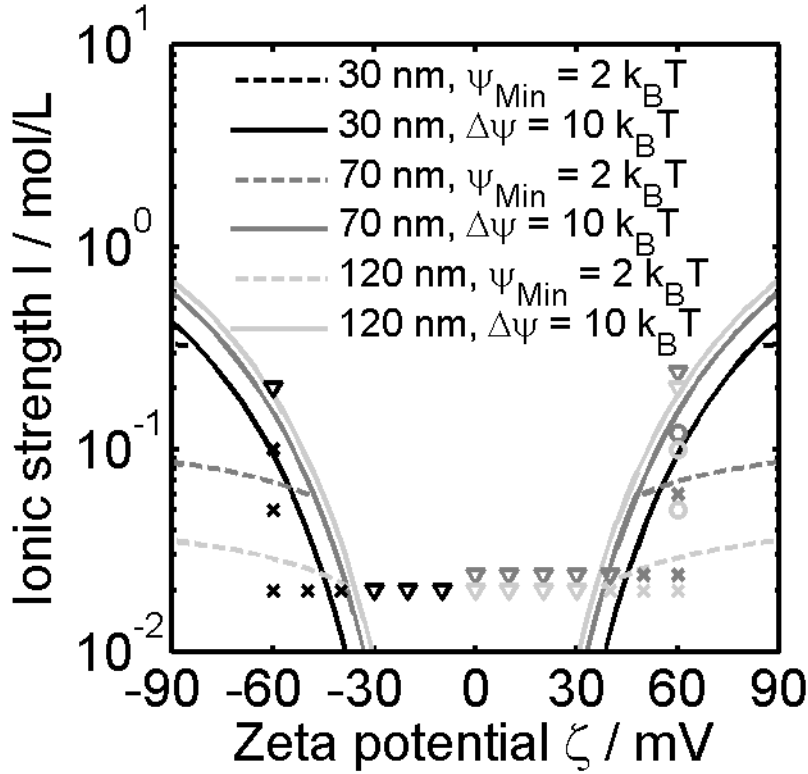


Figure 7: Stability diagram for different particle sizes showing the regions of primary agglomeration (above the solid lines), secondary agglomeration (between the solid and the dashed lines) and stable suspensions (below the dashed lines). The agglomeration behavior observed in the simulations is indicated by triangles (primary agglomerates), circles (secondary agglomerates), and crosses (stable suspensions) for particle diameters of 30 nm (black symbols), 70 nm (dark grey symbols), and 120 nm (light grey symbols). The data points for a particle diameter of 70 nm are shifted vertically for the sake of clarity.

The simulations start with statistically distributed particles which move and agglomerate due to Brownian motion. Before the filtration starts, the agglomeration must come to an equilibrium state, which is controlled via the evolution of the pair correlation function. Beginning with a completely irregular structure, the nearest-neighbor peaks evolve rapidly. The peaks for higher orders follow and reach their equilibrium values after about 0.7 ms for a particle diameter of 30 nm, 4.4 ms for a particle diameter of 70 nm, and 30 ms for a particle diameter of 120 nm. The agglomeration time is longer for larger particles because of the slower Brownian motion, but this also permits larger time steps. The filtration starts directly after the specified agglomeration times since a longer agglomeration would primarily increase the computational time.

6.2. Porosity

After the agglomeration reaches its equilibrium, the filtration starts by incrementally reducing the MD-simulation space. This procedure is controlled by the integral force exerted on the boundary planes. Filter cakes build up at the upper and lower boundaries of the MD simulation until they eventually merge and get compressed. The resulting structure is evaluated in terms of its porosity Φ , which is a function of the total volume of the particles and the filter cake

$$\Phi = 1 - \frac{\frac{4}{3}\pi R^3 N_{MD}}{A_C h_C}. \quad (33)$$

The thickness of the filter cake h_C should not be determined from the coordinates of the highest and lowest particles because the filter cakes are rough and irregular if agglomerates are present. The resulting statistical uncertainty could be reduced by increasing the number of particles, which would also increase the computational effort. Instead, the thickness of the filter cake is calculated from vertical coordinates $x_{z,m}$ of the particles as

$$h_C = 4 \frac{\sum_{i=1}^N \left| x_{z,m} - \frac{\sum_{m=1}^N x_{z,m}}{N_{MD}} \right|}{N_{MD}} + d_p. \quad (34)$$

The porosity of the filter cakes strongly depends on the ionic strength of the suspension (see figure 8), because the ions reduce the Debye length and thus shield the Coulomb repulsion. Accordingly, the porosity is relatively high at an ionic strength of 0.2 mol/L, where the particles are agglomerated. Below 0.1 mol/L, only few agglomerates are formed because of the high energy barrier. The increase of porosity upon a decrease of the ionic strength from 0.1 mol/L to 0.02 mol/L might be caused by the increasing Debye length: for unagglomerated structures the inter-particle distance depends on the equilibrium of the electrostatic repulsion between the particles and the compressive force on the filter cake. Analogously, the compressibility of filter cakes from colloidal silica spheres decreases with increasing ionic strength as long as it is kept below the critical coagulation concentration⁴⁹. This effect is more pronounced for smaller particles.

A higher pressure during compression results in a lower porosity of the filter cake (see figure 8). The compressibility of the filter cake strongly depends on the internal structure: a stabilized suspension leads to a dense packing even at low compressive loads, while the loose

structure resulting from agglomerated particles can be easily compressed by rearrangement of the particles, so that the agglomerates can be considered as deformable particles. This effect is stronger for smaller particles. The compressibility is negligible at an ionic strength of 0.1 mol/L, where the particles are in very close contact. The compressibility increases again for lower ionic strengths, where the nearest-neighbor particle distance reflects the balance between compression and DLVO interactions.

In the simulations, the compressibility increases with decreasing particle diameter, probably because of the broader primary minimum and thus higher mobility within the agglomerates. However, the effect is not observable in the experiments with irregularly shaped particles and we are not aware of experimental studies comparing ideally spherical particles with different sizes.

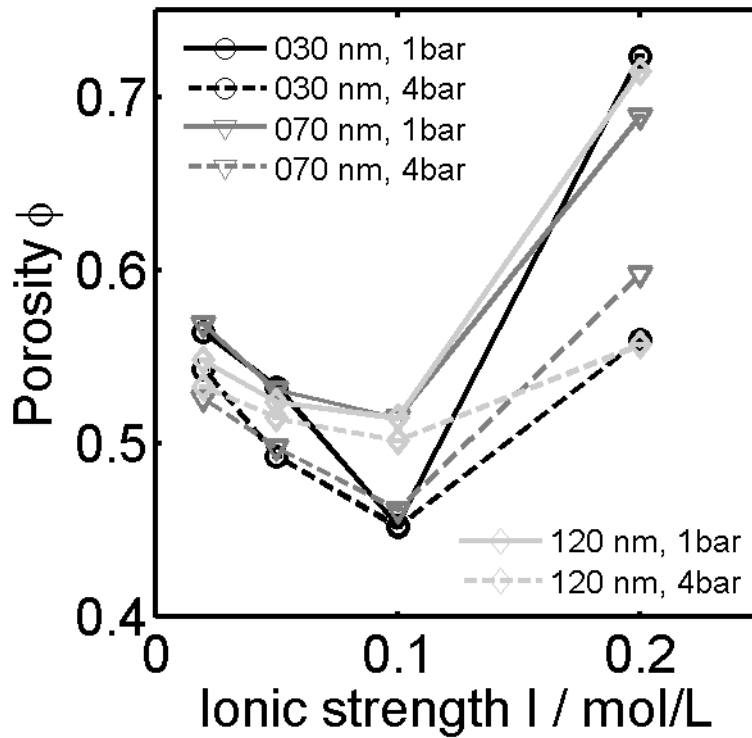


Figure 8: Porosity of the filter cakes depending on the ionic strength of the suspension for different particle diameters and for different compressive loads.

The porosity of the filter cakes also depends on the zeta potential of the particles (see figure 9). At low zeta potentials, the porosity is relatively high for all particle diameters and for all compressive loads because the particles are agglomerated, which is also observed in the experiments⁶⁹. At a zeta potential of 40 mV, the Coulomb repulsion prevents agglomeration, causing a lower porosity. A further increase of the zeta potential increases the repulsion and thus the distance between the particles, in analogy to what happens when the ionic strength is decreased. Also the influence of the compression is analogous.

The error bars at a zeta potential of 0 mV indicate the 95% confidence intervals based on five simulations with different seeds for the random number generator, carried out for each particle diameter and each compressive load. These are the suspected worst cases, since the structures are more regular for stable suspensions.

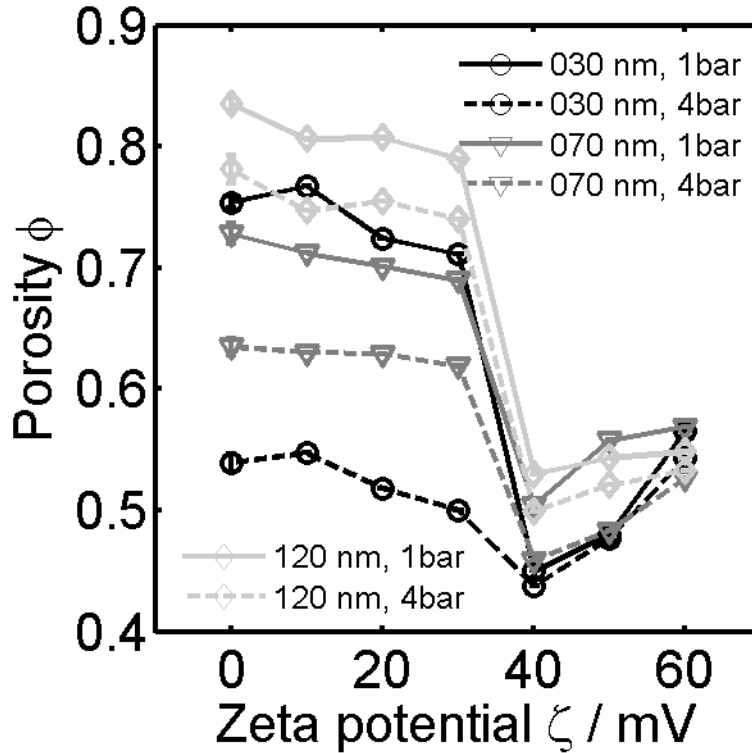


Figure 9: Porosity of the filter cakes depending on the zeta potential of the particles for different particle diameters and for different compressive loads.

6.3. Permeability

Also the permeability of the filter cakes depends on the ionic strength of the suspension (see figure 10), which can be attributed to the changing pore size. The mean velocity in the pores decreases with decreasing pore diameter in the regime of laminar flow. The logarithmic plots of the permeability are similar in shape to the linear plot of the porosity. Upon an increase of the ionic strength, the permeability first decreases because the particles come closer due to the smaller Debye length. Above 0.1 mol/L, where the particles agglomerate, the permeability increases significantly. The permeability also decreases with increasing compression and with decreasing particle size for all ionic strengths. The pores between the particles are smaller for smaller particles if the porosity is identical.

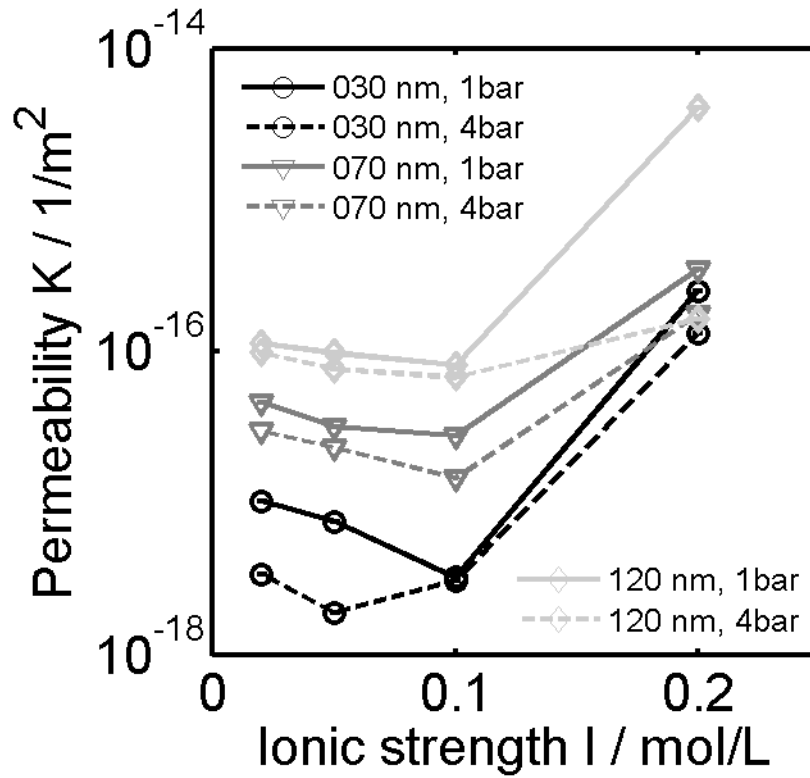


Figure 10: Permeability of the filter cakes depending on the ionic strength of the suspension for different particle diameters and for different compressive loads.

Figure 11 shows the permeability for a variation of the zeta potential. The permeability decreases with increasing compression and with decreasing particle size. Upon increasing the zeta potential up to 40 mV, the permeability decreases because of the decreasing porosity. Beyond 40 mV, the permeability increases again, especially for the smallest particles. This effect is also stronger for weaker compression.

Again, the error bars are shown for the suspected worst cases, which are the packed beds resulting from agglomerated particles with a zeta potential of 0 mV. The 95% confidence intervals are based on five simulations with different seeds for the random number generator, carried out for each particle diameter and each compressive load.

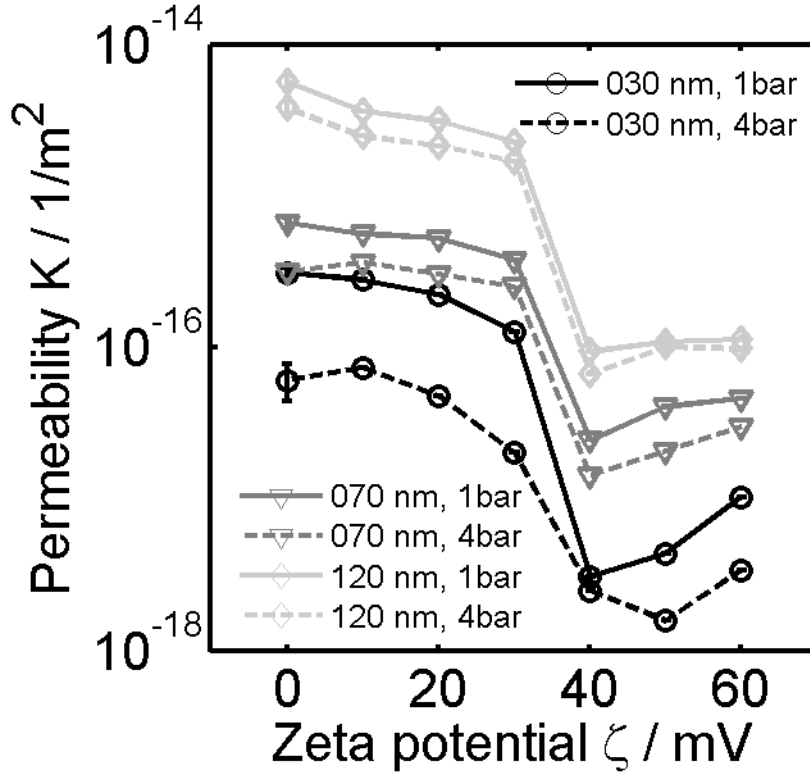


Figure 11: Permeability of the filter cakes depending on the zeta potential of the particles for different particle diameters and for different compressive loads.

The lattice Boltzmann (LB) simulations reveal that, for each particles size, the permeability of a packed bed is an exponential function of its porosity, which itself depends on the zeta potential, the ionic strength, and the compressive loads (see figure 12). A significant deviation from the exponential relation between the porosity and the permeability is found only for the 30 nm particles, where the simulated permeabilities are too high for porosities around 0.55. This indicates a stronger influence of the pore size heterogeneity on the permeability for smaller particles.

The simulated permeabilities can be approximated by an exponential function of the porosity

$$K = a \cdot e^{b \cdot \Phi}, \quad (35)$$

with the coefficients a and b given in table 2 for the different particle sizes. The influence of the porosity, as given by the coefficient b , is similar for the different particle sizes, with values between 13.7 and 15.6. The parameter a reflects the higher permeability of packed beds composed of larger particles.

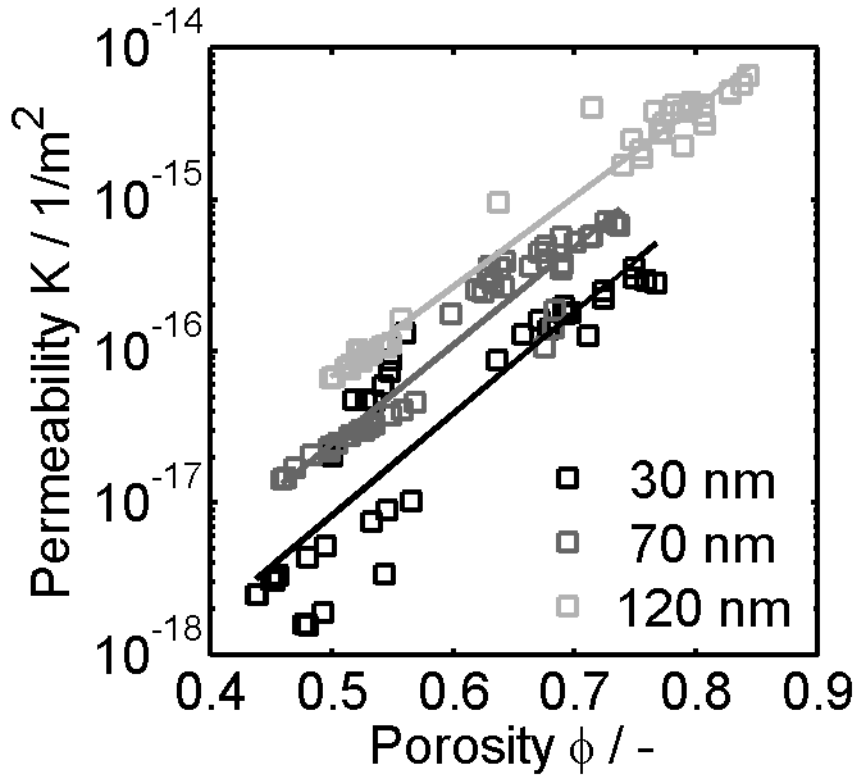


Figure 12: Permeability depending on the porosity for different particle diameters as resulting from the simulations.

Similar exponential relations between the porosity and the permeability are found in the experiments on the permeability of filter cakes consisting of colloidal boehmite particles (see figure 13). The influence of the porosity, which is contained in the parameter b , is again similar for the different particle sizes and the experiments are very close to the simulations. The deviation of the coefficient a is caused by the polydispersity and the non-spherical form of the particles in the experiment. While for the monodisperse spheres in the simulation, the regimes of stable and agglomerates particles can be clearly separated, the irregular shape of the particles in the experiments smoothes the transition between the agglomerated and unagglomerated state.

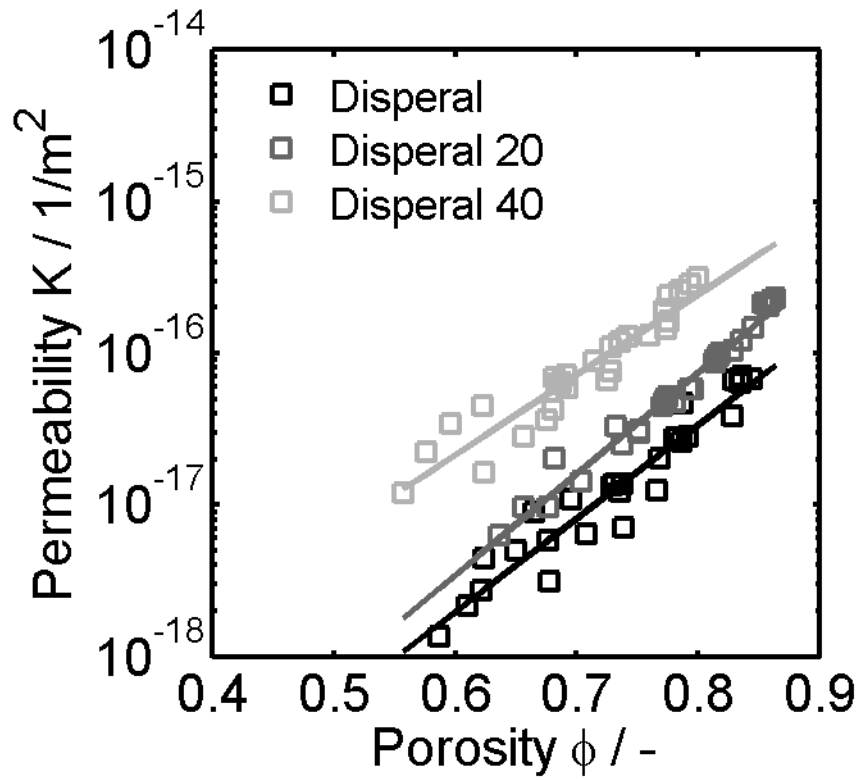


Figure 13: Permeability depending on the porosity for different particle diameters as resulting from the experiments.

Table 2: Coefficients for the permeability as a function of the porosity

Particle diameter	Simulation		Experiment	
	a	b	a	b
30 nm	$3,3 \cdot 10^{-21}$	15,6	$4.85 \cdot 10^{-22}$	13.9
70 nm	$2 \cdot 10^{-20}$	14,2	$6 \cdot 10^{-22}$	14.7
120 nm	$7 \cdot 10^{-20}$	13.7	$2.9 \cdot 10^{-20}$	11.3

7. Summary

Agglomeration and filtration of colloidal particles are investigated with a simulation method that combines molecular dynamics (MD) with stochastic rotation dynamics (SRD).

The agglomeration of the simulated particles depends on their zeta potential and the ionic strength of the suspension, as predicted by the DVLO theory. Analyzing the pair correlation function permits to determine the time for the agglomeration to reach equilibrium and to distinguish between primary and secondary agglomerates. The following filtration and compression is realized by reducing the simulation space incrementally. The porosity of the resulting filter cake depends on the compressive load and the agglomeration of the particles and agrees qualitatively with experimental results for particles in the same size range. Discrepancies are mainly attributed to the non-spherical form of the real particles and the smaller system size.

The permeabilities of the fixed filter cake structures are determined by lattice Boltzmann (LB) simulations. For each particle size, the permeability is found to be an exponential function of the porosity, which is also found in experimental investigations.

8. Acknowledgements

We thank the German Science Foundation (DFG) for funding within the priority program SPP 1164. The Jülich Supercomputing Center and the Scientific Supercomputing Center Karlsruhe are acknowledged for providing the required computing time.

9. Symbols (for the referee)

a	Coefficient	k_B	Boltzmann constant
A_C	Filter cake cross section area	K	Permeability
A_H	Hamaker constant	K_{Hertz}	Hertz constant
Ar	Archimedes number	Kn	Knudsen number
b	Coefficient	L_z	Dimension of the simulation space in vertical direction
Bo	Boltzmann number	L_{Cell}	Length of the SRD cells
c_{Lub}	Lubrication constant	m	Mass
c_s	Speed of sound	m_m	Mass of the particle m
d	Distance between the particle centers	m_{SRD}	Mass of one SRD particle
$d_{50,0}$	Number-rated average particle diameter	M	Molecular mass of the fluid
d_p	Particle diameter	Ma	Mach number
D	Diffusion constant	N	Number of particles
D_H	Hooke constant	N_k	Number of particles in SRD cell k
e	Elementary charge	$\langle N_k \rangle$	Average number of SRD particles per cell
\mathbf{e}_j	Lattice vectors	N_A	Avogadro constant
F	Faraday constant	N_{MD}	Number of MD particles
\mathbf{F}_m	Force on particle m	Pe	Péclet number
F_{Lub}	Lubrication force	R_C	Cake resistance
f_j	Boltzmann distribution function for lattice vector \mathbf{e}_j	$r_{CO,i}$	Inner cut-off radius
f_j^{eq}	Equilibrium distribution function for lattice vector \mathbf{e}_j	R_F	Flow resistance
g	Gravitational constant	R_M	Membrane resistance
G	Pair correlation function	Re	Reynolds number
h_c	Thickness of the filter cake	Sc	Schmidt number
I	Ionic strength	t	Time
		T	Temperature
		T_{SRD}	Temperature of the SRD fluid
		v_{LB}	Macroscopic velocity

\mathbf{v}_{Sed}	Stokes velocity	ρ_{LB}	LB density
V	Simulation volume	ρ_s	Solid density
\dot{V}_L	Volume flux	τ_{Diff}	Diffusion time
w_j	Lattice weights	τ_L	Liquid relaxation time
\mathbf{x}_m	Position of particle m	τ_{LB}	LB relaxation time
$\mathbf{x}_{z,m}$	Position of particle m	τ_p	Particle relaxation time
$\dot{\mathbf{x}}_m$	Velocity of particle m	τ_{Sed}	Sedimentation time
$\dot{\bar{\mathbf{x}}}_k$	Mean velocity of the particles in the cell k	τ_{TF}	Thermal fluctuation time
$\ddot{\mathbf{x}}_m$	Acceleration of particle m	$\Omega_{LB,j}$	LB collision operator for lattice vector \mathbf{e}_j
z	Ion valency	$\Omega_{SRD,k}$	SRD rotation matrix for cell k
Greek symbols		Ψ_{vdW}	Van-der-Waals potential
Δp	Pressure difference	Ψ_{Coul}	Coulomb potential
Δt_{LB}	Time step	Ψ_{Hertz}	Hertz potential
Δt_{SRD}	Time step	ζ	Zeta potential
ϵ_0	Vacuum permittivity	Indices	
ϵ_{rel}	Relative permittivity	i	Index
Φ	Porosity	j	Index for lattice vectors
ϕ_j	Additional forces term in LB	k	Index for cells
η	Dynamic viscosity of the permeate	m	Index for particles
η_{SRD}	Dynamic viscosity of the SRD fluid	n	Index for particles
κ	Reciprocal Debye length	C	Cake
λ	Mean free path of the SRD particles	L	liquid
ρ°	Reference density	S	solid
ρ_L	Liquid density		

10. References

1. J. Kocurek; M. Palica, *Powder Technology* **2005**, 159, (1), 17-26.
2. R. Konnur; S. Raha; J. Tanwar; S. Phanikanth; Pradip; P. C. Kapur, *Drying Technology* **2008**, 26, (8), 1044-1059.

3. J. Olivier; J. Vaxelaire; E. Vorobiev, *Separation Science and Technology* **2007**, 42, (8), 1667-1700.
4. P. K. Park; C. H. Lee; S. Lee, *Environmental Science Technology* **2006**, 40, (8), 2699-2705.
5. A. S. Kim; R. Yuan, *Journal of Membrane Science* **2005**, 249, (1-2), 89-101.
6. A. S. Kim; R. Yuan, *Journal of Membrane Science* **2006**, 286, (1-2), 260-268.
7. H.-W. Lao; H. J. Neeman; D. V. Papavassiliou, *Chemical Engineering Communications* **2004**, 191, (10), 1285-1322.
8. B. Einfeld; K. Schnitzlein, *Chemical Engineering Science* **2005**, 60, (15), 4105-4117.
9. B. Wachmann; W. Kalthoff; S. Schwarzer; H. J. Herrmann, *Granular Matter* **1998**, 1, (2), 75-82.
10. W. Kalthoff; S. Schwarzer; H. J. Herrmann, *Physical Review E* **1997**, 56, (2), 22342242.
11. N. Olivi-Tran; P. Lenormand; A. Lecomte; A. Dager, *Physica A* **2005**, 354, 10-18.
12. A. S. Kim; E. M. V. Hoek, *Environmental Engineering Science* **2002**, 19, (6), 373-386.
13. M. Barcenas; J. Douda; Y. Duda, *Journal of Chemical Physics* **2007**, 127, (11), 114706.
14. B. M. Yu; M. Q. Zou; Y. J. Feng, *International Journal of Heat and Mass Transfer* **2005**, 48, (13), 2787-2794.
15. J. Cordelair; P. Greil, *Journal of the European Ceramic Society* **2004**, 24, (9), 2717-2722.
16. M. Hütter, *Journal of Colloid and Interface Science* **2000**, 231, (2), 337-350.
17. J. R. Melrose; D. M. Hexes, *Journal of Chemical Physics* **1993**, 98, (7), 5873-5886.
18. J. C. Kim; K. H. Auh, *Modelling and Simulation in Materials Science and Engineering* **1999**, 7, (3), 447-458.
19. J. F. Brady; G. Bossis, *Annual Review of Fluid Mechanics* **1988**, 20, (1), 111-157.
20. A. Sierou; J. F. Brady, *Journal of Fluid Mechanics*, 448 . pp. 115-146. ISSN 0022-1120 **2001**.
21. J. Harting; M. Hecht; H. J. Herrmann; S. McNamara, *Computer Simulation of Particle Suspensions*. Springer: 2006.
22. J. T. Padding; A. A. Louis, *Physical Review E* **2006**, 74, (3), 031402.
23. R. Adhikari; K. Stratford; M. E. Cates; A. J. Wagner, *Europhysics Letters* **2005**, 71, (3), 473-479.
24. B. Dunweg; U. D. Schiller; A. J. C. Ladd, *Physical Review E* **2007**, 76, (3), 036704-10.
25. A. Malevanets; R. Kapral, *The Journal of Chemical Physics* **1999**, 110, (17), 8605-8613.
26. J. T. Padding; A. A. Louis, *Physical Review Letters* **2004**, 93, (22), 220601.
27. M. Hecht; J. Harting; T. Ihle; H. J. Herrmann, *Physical Review E* **2005**, 72, (1), 011408.
28. Y. Inoue; Y. Chen; H. Ohashi, *Journal of Statistical Physics* **2002**, 107, (1), 85-100.
29. M. Hecht; J. Harting; H. J. Herrmann, *Physical Review E* **2007**, 75, (5), 051404.
30. E. S. Boek; H. K. Ladva; J. P. Crawshaw; J. T. Padding, *Energy Fuels* **2008**, 22, (2), 805-813.
31. R. G. Winkler; K. Mussawisade; M. Ripoll; G. Gompper, *Journal of Physics: Condensed Matter* **2004**, 16, (38), 3941-3954.
32. Y. Efendiev; T. Hou; T. Strinopoulos, *Computational Geosciences* **2008**, 12, (3), 257-272.
33. M. Madadi; M. Mehrabi, *Proceedings of the 4th International Conference on Nanochannels, Microchannnels, and Minichannels* **2006**, 953-957.

34. B. V. Derjaguin; L. Landau, *Acta Phys. Chim. URSS* - 662 **1941**, 14, 633.
35. E. J. W. Verwey; J. T. G. Overbeek, *Theory of the Stability of Lyophobic Colloids*. Elsevier: Amsterdam, 1948.
36. H. Darcy, *Les Fontaines Publiques de la Ville de Dijon*. Dalmont: Paris, 1856.
37. S. Biggs, *Kona* **2006**, 24, 41-53.
38. M. H. Cho; C. H. Lee; S. Lee, *Desalination* **2006**, 191, (1-3), 386-396.
39. S. Raha; K. C. Khilar; P. C. Kapur; Pradip, *International Journal of Mineral Processing* **2007**, 84, (1-4), 348-360.
40. J. Lyklema, *Fundamentals of interface and colloid science*. Academic Press: London, 1995.
41. R. J. Hunter, *Introduction to modern colloid science*. Oxford University Press: Oxford, 1993.
42. T. Cosgrove, *Colloid Science: Principles, Methods and Applications*. Blackwell Pub: Oxford, UK, 2005; p xvi, 288 p.
43. H. C. Hamaker, *Physica* **1937**, 4, 1058-1072.
44. J. Lyklema, *Fundamentals of interface and colloid science*. Academic Press: London, UK, 1993.
45. P. W. Atkins; J. De Paula, *Atkins' Physical chemistry*. Oxford University Press: Oxford, 2006.
46. W. M. Lu; K. L. Tung; S. M. Hung; J. S. Shiau; K. J. Hwang, *Powder Technology* **2001**, 116, (1), 1-12.
47. J. B. Madeline; M. Meireles; R. Botet; B. Cabane, *Water Science and Technology* **2006**, 53, (7), 25-32.
48. C. Selomulya; X. Jia; R. A. Williams, *Chemical Engineering Research and Design* **2005**, 83, (A7), 844-852.
49. G. Singh; L. Song, *Industrial und Engineering Chemistry Research* **2006**, 45, (22), 7633-7638.
50. M. P. Allen; D. J. Tildesley, *Computer simulation of liquids*. Clarendon Press: Oxford, 1987.
51. M. Hecht; J. Harting; M. Bier; J. Reinshagen; H. J. Herrmann, *Physical Review E* **2006**, 74, (2), 021403.
52. T. Ihle; D. M. Kroll, *Physical Review E* **2003**, 67, (6), 066705.
53. A. Einstein, *Investigations on the theory of the Brownian movement*. Dover Publications: Mineola, USA, 1956.
54. G. Wedler, *Lehrbuch der physikalischen Chemie*. Wiley-VCH: Weinheim, Germany, 2007.
55. A. Narvaez; T. Zauner; F. Raischel; J. Harting; R. Hilfer, **2009**.
56. X. He; L.-S. Luo, *Physical Review E* **1997**, 56, (6), 6811-6817.
57. P. L. Bhatnagar; E. P. Gross; M. Krook, *Physical Review* **1954**, 94, (3), 511-525.
58. R. Benzi; S. Succi; M. Vergassola, *Physics Reports* **1992**, 222, (3), 145-197.
59. X. He; L.-S. Luo, *Journal of Statistical Physics* **1997**, 88, (3), 927-944.
60. O. Dardis; J. McCloskey, *Physical Review E* **1998**, 57, (4), 4834-4837.
61. A. P. Deshpande; A. Srikanth; N. Praveen, *Canadian Journal of Chemical Engineering* **2005**, 83, (5), 808-815.
62. U. Aaltosalmi. Fluid flow in porous media with the lattice-Boltzmann method. University of Jyväskylä, Finland, 2005.
63. C. Manwart; U. Aaltosalmi; A. Koponen; R. Hilfer; J. Timonen, *Physical Review E* **2002**, 66, (1), 016702.
64. S. Chen; G. D. Doolen; K. G. Eggert, *Los Alamos Science* **1994**, 22, 98-111.
65. Z. Guo; C. Zheng; B. Shi, *Physical Review E* **2002**, 65, (4), 046308.
66. I. Ginzburg; D. d'Humières, *Physical Review E* **2003**, 68, (6), 066614.

67. P. Lallemand; L.-S. Luo, *Physical Review E* **2003**, 68, (3), 036706.
68. C. Pan; L.-S. Luo; C. T. Miller, *Computers and Fluids* **2006**, 35, (8), 898-909.
69. B. Schäfer; H. Nirschl, *Physical Separation in Science and Engineering* **2009**, 2009, 1-9.
70. B. Schäfer; H. Nirschl, *Journal of Colloid and Interface Science* **2008**, 318, (2), 457-462.